

# The SRG/eROSITA all-sky survey

## View of the Fornax galaxy cluster

T.H. Reiprich<sup>1</sup>, A. Veronica<sup>1</sup>, F. Pacaud<sup>1</sup>, P. Stöcker<sup>1</sup>, V. Nazaretyan<sup>1</sup>, A. Srivastava<sup>1</sup>, A. Pandya<sup>1</sup>, J. Dietl<sup>1</sup>, J.S. Sanders<sup>2</sup>, M.C.H. Yeung<sup>2</sup>, A. Chaturvedi<sup>3</sup>, M. Hilker<sup>4</sup>, B. Seidel<sup>5</sup>, K. Dolag<sup>5</sup>, J. Comparat<sup>2</sup>, V. Ghirardini<sup>6,2</sup>, M. Kluge<sup>2</sup>, A. Liu<sup>7,2</sup>, N. Malavasi<sup>2</sup>, X. Zhang<sup>2</sup>, and E. Hernández-Martínez<sup>5</sup>

<sup>1</sup> Argelander-Institut für Astronomie (AIfA), Universität Bonn, Auf dem Hügel 71, 53121 Bonn, Germany

<sup>2</sup> Max-Planck-Institut für extraterrestrische Physik, Gießenbachstr. 1, 85748 Garching bei München, Germany

<sup>3</sup> Leibniz-Institut für Astrophysik Potsdam (AIP), An der Sternwarte 16, D-14482 Potsdam, Germany

<sup>4</sup> European Southern Observatory, Karl-Schwarzschild-Straße 2, 85748 Garching, Germany

<sup>5</sup> Universitäts-Sternwarte, Fakultät für Physik, Ludwig-Maximilians-Universität München, Scheinerstr. 1, 81679 München, Germany

<sup>6</sup> INAF, Osservatorio di Astrofisica e Scienza dello Spazio, via Piero Gobetti 93/3, 40129 Bologna, Italy

<sup>7</sup> Institute for Frontiers in Astronomy and Astrophysics, Beijing Normal University, Beijing 102206, China

Received ...; accepted ...

### ABSTRACT

**Context.** The Fornax cluster is one of the most nearby X-ray bright galaxy clusters, allowing us to study the system at high spatial resolution. However, previous observations of the intracluster medium were limited to less than  $R_{500}$ .

**Aims.** We aim to significantly extend the X-ray coverage of the Fornax cluster and to search for features in the X-ray surface brightness distribution beyond  $R_{500}$  induced by the gravitational growth of this system.

**Methods.** We use data from five SRG/eROSITA all-sky surveys and perform a detailed one- and two-dimensional X-ray surface brightness analysis, allowing us to trace hot gas emission from kpc to Mpc scales with a single instrument. We compare the results to those from a recent numerical simulation of the local Universe (SLOW) and correlate the X-ray emission distribution with that of other tracers, including cluster member galaxies, ultra compact dwarf galaxies, intracluster globular clusters, and HI-tail galaxies.

**Results.** We detect X-ray emission out to well beyond the virial radius,  $R_{100} = 2.2$  deg. We do not find obvious evidence for the bow shock several hundred kpc south of the cluster center predicted by previous numerical simulations of the Fornax cluster. Instead, we discover finger-like structures beyond  $R_{500}$  to the west and south-east that stretch out far beyond the virial radius. They might be due to gas being pushed outward by the previous merger with NGC 1404 or due to warm-hot gas infall along large-scale filaments. Intriguingly, we find the distributions of the other tracers – galaxies and globular clusters – to be correlated with the X-ray excess regions, favoring the latter infall scenario. Interestingly, we also discover an apparent Bridge of low surface brightness emission beyond the virial radius connecting to the Fornax A galaxy group, which is also traced by the member galaxy and globular cluster distribution. This X-ray Bridge furthermore approximately coincides with a region of enhanced Faraday depth detected previously. The gas distribution in the SLOW simulation shows similar features as those we have discovered with SRG/eROSITA.

**Conclusions.** SRG/eROSITA has allowed us to tremendously expand the view of the intracluster medium of the Fornax cluster. We witness the growth of a cluster along large-scale filaments.

**Key words.** Galaxies: clusters: individual: Fornax cluster – X-rays: galaxies: clusters - intergalactic medium

## 1. Introduction

With a virial diameter of almost 4.5 deg, the Fornax cluster is one of the most extended clusters of galaxies in the sky. In fact, only the Virgo cluster (e.g., McCall et al. 2024) spans a larger area. The apparent large extent is due to their proximity. Their intrinsic physical sizes, i.e., masses, are actually not extraordinary; in fact, the Fornax cluster should rather be called a group of galaxies based on its mass of  $<10^{14} M_{\odot}$  (e.g., Jones et al. 1997; Drinkwater et al. 2001; Reiprich & Böhringer 2002; Piffaretti et al. 2011; Smith Castelli et al. 2024). Given its proximity, the Fornax cluster can be studied at high spatial resolution and down to low surface brightness at all wavelengths. And, indeed, it is one of the best studied galaxy clusters in existence. In particular, its two central bright elliptical galaxies, NGC 1399 and NGC 1404, as well as the central galaxy of the neighbor-

ing Fornax A galaxy group, NGC 1316, have been the subject of many previous studies.

For example, Su et al. (2017b) used a mosaic of 15 XMM-Newton observations (see also Murakami et al. 2011) and Chandra observations to describe four contact discontinuities identified as sloshing cold fronts (for a review about cold fronts see, e.g., Markevitch & Vikhlinin 2007). They suggest these cold fronts are caused by the infall of NGC 1404.

Deep Chandra data have been used to study NGC 1404 at high spatial resolution, resulting in the findings of a sharp contact discontinuity to the north-west, i.e., in the direction of NGC 1399 at the center of the Fornax cluster, and a tail to the south-east (e.g., Machacek et al. 2005; Su et al. 2017a), consistent with NGC 1404 falling into the core of the Fornax cluster as already indicated by ROSAT PSPC data (Jones et al. 1997).

Sheardown et al. (2018) then used detailed hydrodynamic simulations to study if a presumed infall of NGC 1404 could

give rise to the central ICM morphology of the Fornax cluster, e.g., the cold fronts described above as well as the contact discontinuity and tail of NGC 1404. And, indeed, they found the most likely scenario to be that NGC 1404 is on its second or third encounter with the Fornax center. Furthermore, they predicted a detached bow shock 450 kpc to 750 kpc south of NGC 1404. With the eROSITA data used here, we put this prediction to the test.

NGC 1316 is the central galaxy of a group of galaxies that, based on galaxy dynamics, appears to be bound to the Fornax cluster and infalling to it for the first time (Drinkwater et al. 2001). This group is dominated by late-type galaxies and its low fraction of intra-group light points to an ongoing phase of pre-processing (Raj et al. 2020). NGC 1316 is also host to the well-known Fornax A extended radio source and its radio morphology is consistent with a northward, i.e., infalling motion (e.g., Ekers et al. 1983). Recently, Anderson et al. (2021) studied the Faraday depth in a large field surrounding the Fornax cluster using a large number of background sources (see also Loi et al. 2025 for a smaller but more densely sampled Faraday Rotation Measure grid). Anderson et al. found a region of increased Faraday depth north-east of NGC 1316, i.e., in the direction of NGC 1399. In the light of these findings, it is of interest to search for warm-hot gas emission beyond the virial radius of the Fornax cluster towards the direction of Fornax A, which is what we do with the eROSITA data analyzed here.

Given their higher velocity dispersion compared to big galaxies, Drinkwater et al. (2001) concluded that the dwarf galaxy population includes many infalling objects. Indeed, the spatial distribution of dwarf galaxies in the main Fornax cluster is highly structured along clumpy overdensities (e.g., Ordenes-Briceño et al. 2018). The distribution of dwarf galaxies in the infalling Fornax A group is lopsided towards the main cluster, further supporting recent interaction between both components (Su et al. 2021). Given these findings, it is, therefore, of interest to compare the spatial distribution of dwarf galaxies with regions of excess X-ray emission and the warm-hot gas distribution in the cluster outskirts, which may indicate preferred filamentary inflow directions.

Furthermore, we also compare these to the globular cluster and normal galaxy distributions. The inhomogeneous and partly patchy spatial distribution of the intracluster light (Iodice et al. 2016, 2017) and globular clusters (D’Abrusco et al. 2016; Cantiello et al. 2020) within the virial radius trace the recent assembly history of the Fornax cluster. Kinematically cold substructures of intracluster globular clusters (Schuberth et al. 2008; Chaturvedi et al. 2022; Napolitano et al. 2022) support the assembly of the cluster along filaments.

The X-ray telescope eROSITA (Predehl et al. 2021) onboard the Spectrum-Roentgen-Gamma (SRG) satellite (Sunyaev et al. 2021) has performed four all-sky surveys up to now plus one partial sky survey. The data of the first all-sky survey and the corresponding X-ray source catalog is published (Merloni et al. 2024). Given the unlimited field-of-view, these data are perfectly suited to study the very extended Fornax cluster and its surroundings. In this paper, we use data from five surveys.

According to the MCXC database (Piffaretti et al. 2011) the Fornax cluster is located at R.A. = 54.6163 and Dec. = -35.4483 (J2000) at a redshift of 0.005 and has  $R_{500} = 1.06$  deg = 393 kpc.  $R_{500}$  is the radius within which the mean total density equals 500 times the critical density. Using the conversion in Reiprich et al. (2013), this implies  $R_{200} = 1.63$  deg = 604 kpc and  $R_{100} = 2.22$  deg = 816 kpc; i.e., the virial region of the Fornax cluster spans almost 4.5 deg across. The Fornax cluster lies projected in a re-

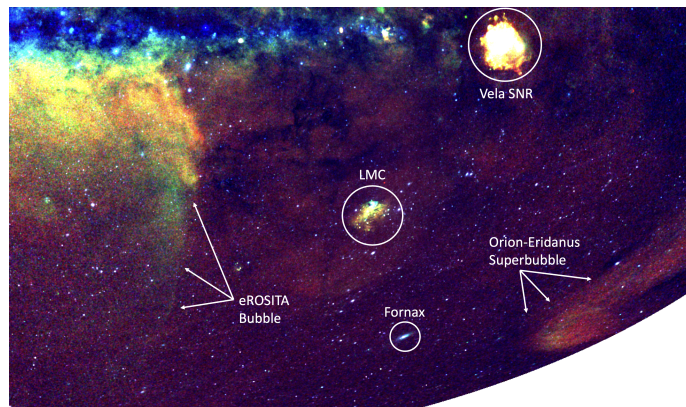


**Fig. 1.** eRASS1 broadband maps in Galactic coordinates from Zheng et al. (2024) in the energy bands 0.4–0.6 keV (red), 0.6–1.0 keV (green), and 1.0–2.3 keV (blue). Some prominent extended sources are labelled, including the Large Magellanic Cloud (LMC). The nearby bright Fornax cluster lies in a particularly benign X-ray background region, optimally placed for studies of its low surface brightness outskirts.

gion of the sky that features a rather simple X-ray background structure (Fig. 1)<sup>1</sup> allowing us to perform a robust background treatment despite the large extent.

For the flat cosmology with  $\Omega_m = 0.3$  and  $H_0 = 70$  km/s/Mpc, assumed throughout this paper, and for a redshift of 0.005, 1 arcsec corresponds to 0.103 kpc.

## 2. eROSITA data reduction and analysis

Since we are interested in the faintest cluster outskirts emission regions, we take advantage of eROSITA data from all five currently existing sky surveys, based on processing version c020. For the data reduction, we use eSASS (Brunner et al. 2022) version users\_211214.0.4.

We follow closely the steps described in detail in Reiprich et al. (2021); Veronica et al. (2024, 2025); McCall et al. (2024); Dietl et al. (2024). Therefore, we do not repeat the description of these steps here but only briefly outline them.

We employ a sufficient number of tiles around the Fornax cluster center to cover area at least out to  $\sim 2R_{100}$  in all directions. We use data from all seven telescope modules (TMs) and apply the parameters `pattern=15` and `flag=0xe00fff30` when running `evttool`. We use the latter strict flag filtering since we are mostly interested in the faintest regions, requiring the cleanest data.<sup>2</sup> We run `flaregti` using photons with energy above 5 keV and setting a  $3\sigma$  threshold for the lightcurve filtering. Then, images and exposure maps are created in the energy band 0.2–2.3 keV (0.8–2.3 keV) for the TMs with (without) on-chip filter (Predehl et al. 2021). To generate false color (RGB) images, also images and exposure maps in additional bands are created. The final images are fully corrected: (i) the particle-induced background (PIB; Freyberg et al. 2020; Yeung et al. 2023) is subtracted; (ii) a relative correction for the varying foreground absorption in the field is performed using data from HI4PI Collaboration et al. (2016); (iii) the different TM sensitivities and energy bands are taken into account for the total exposure correction, including vignetting.

<sup>1</sup> [https://erosita.mpe.mpg.de/dr1/AllSkySurveyData\\_dr1/HalfSkyMaps\\_dr1/](https://erosita.mpe.mpg.de/dr1/AllSkySurveyData_dr1/HalfSkyMaps_dr1/)

<sup>2</sup> See [https://erosita.mpe.mpg.de/edr/DataAnalysis/prod\\_descript/EventFiles\\_edr.html](https://erosita.mpe.mpg.de/edr/DataAnalysis/prod_descript/EventFiles_edr.html) for details on flag settings.

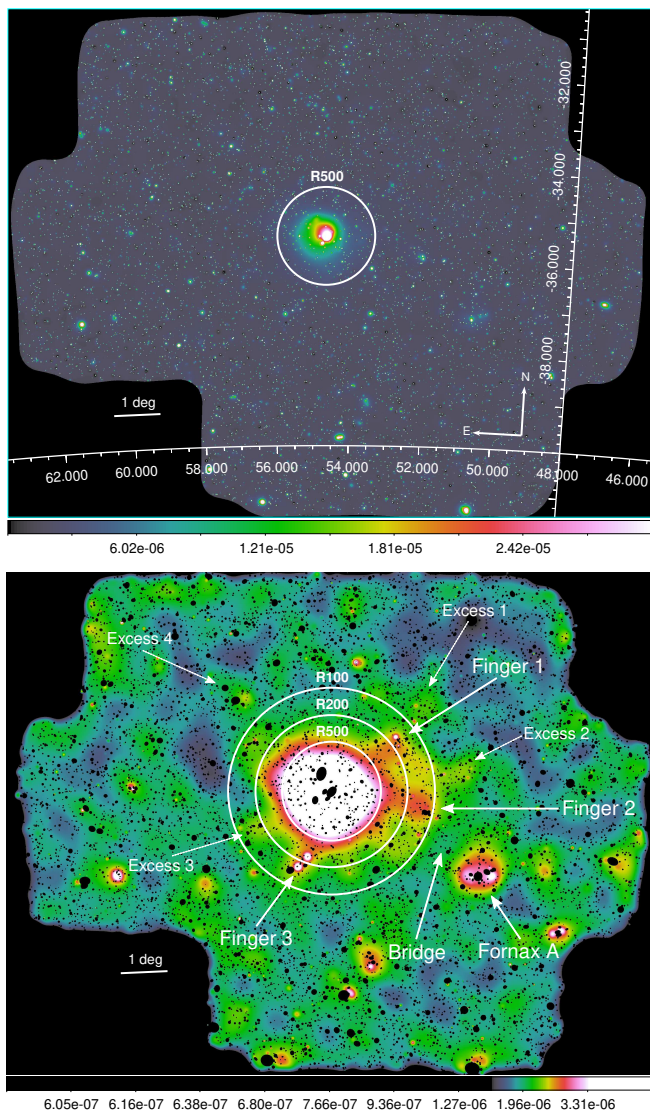


**Fig. 2.** Fully corrected, wavelet-filtered image in the energy band 0.2–2.3 keV; characteristic radii are overlaid. Top: linear scale to enhance central surface brightness structure. Bottom: log scale to enhance outer low surface brightness structure; sources of small extent excised. Also, emission features are labeled that are described in the text.

Since we are primarily interested in very low surface brightness regions, we perform wavelet-filtering to reduce the noise in the final images as described in Reiprich et al. (2021), using an implementation by F. Pacaud of the filtering method in the MR/1 software (Starck & Pierre 1998). For some images, we excise sources detected with SExtractor (Bertin & Arnouts 1996) on the wavelet-filtered images, exploiting the elliptical shape information. Figure 2 shows two image versions resulting from this process.

In addition to qualitative imaging analyses we perform quantitative X-ray surface brightness analyses. We generate exposure- and relative absorption-corrected, PIB-subtracted, and compact source-excised surface brightness profiles in various sectors out to  $2R_{100}$ . For the profile analysis, we decrease the region of the SExtractor-detected source at the center of the Fornax cluster/NGC 1399 to a circle with radius  $30''$  to remove mostly any potential emission from an active nucleus. The level and uncertainty of the X-ray background (CXB) is determined by placing eleven boxes of size 1 deg<sup>2</sup> outside  $\sim 2R_{100}$  and calculating

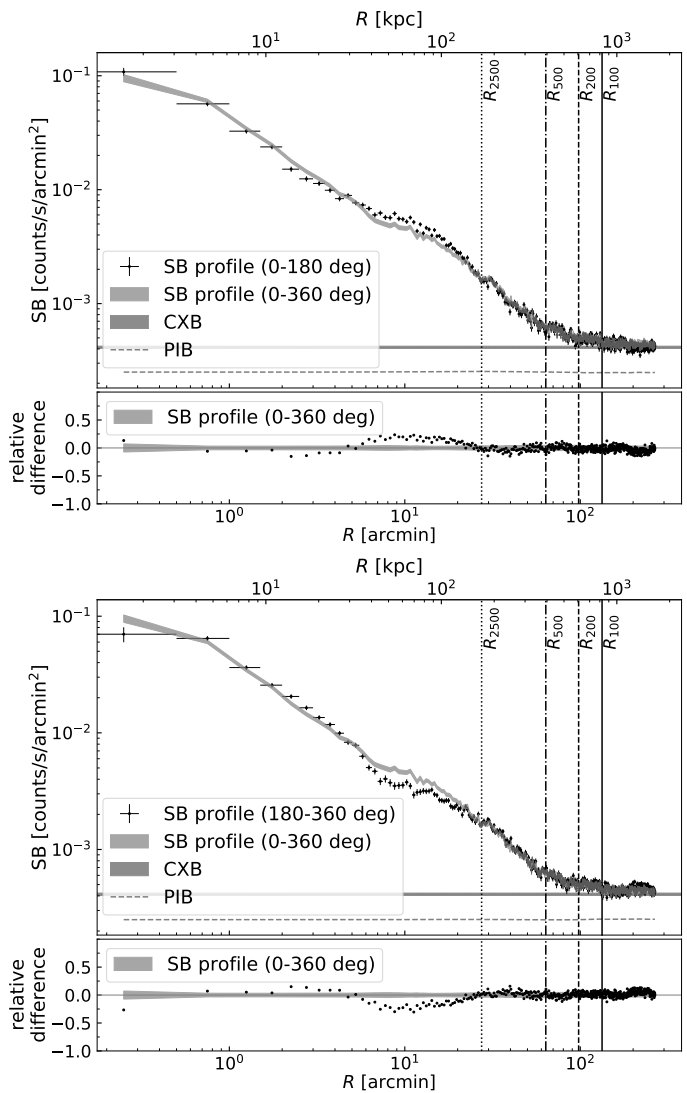


**Fig. 3.** Fully corrected surface brightness profiles for two 180 deg wide sectors in comparison to that from the full (0–360 deg) annuli. PIB is subtracted but not the CXB. Characteristic radii are overlaid. 0 deg is on the right (3 pm), 90 deg on the top (12 pm), 180 deg on the left (9 pm) and 270 deg on the bottom (6 pm).

the average surface brightness and its standard deviation. We use the standard deviation instead of the (smaller) statistical uncertainty based on the number of detected events in order to capture the uncertainty induced by large-scale CXB variations, e.g., due to varying diffuse background emission in our Milky Way. The PIB level in the used 0.2(0.8)–2.3 keV energy band is always well below the CXB level. Two example surface brightness profiles for the sectors 0–180 deg and 180–360 deg, covering scales from  $\sim 3$  kpc to  $\sim 1$  Mpc, are shown in Fig. 3

### 3. Results

#### 3.1. X-ray surface brightness distribution

Focussing first on the core region of the Fornax cluster, we show in Fig. 4 the eROSITA surface brightness overlaid onto an optical color image obtained from the Digitized Sky Survey 2.<sup>3</sup> The X-ray emission peak is centered on NGC 1399. Several other of

<sup>3</sup> <https://www.eso.org/public/images/eso0949m/>

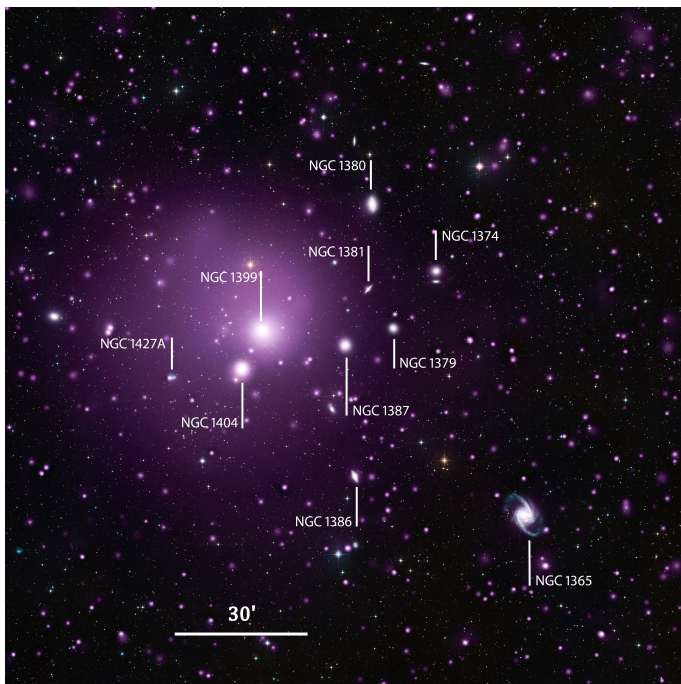


**Fig. 4.** Digitized Sky Survey 2 (DSS2) image of the Fornax cluster in the optical B and R bands. The purple overlay is from the fully corrected eROSITA wavelet-filtered image, on Asinh (hyperbolic arcsine) scale. The big elliptical galaxy close to the center of the image is NGC 1399; the second brightest galaxy in the image about 13' south-south-east is NGC 1404. Other prominent member galaxies are labeled in white. NGC 1316, the central galaxy of the Fornax A group, is further to the south-west, outside the field shown here. Image credits: ESO and Digitized Sky Survey 2. Acknowledgment: Davide De Martin

the bright Fornax member galaxies show X-ray emission, the brightest one being NGC 1404. Furthermore, we observe characteristic features that could be due to sloshing as described in Sect. 1.

To highlight these features more clearly, we show in Fig. 5 a false color wavelet-filtered eROSITA RGB image based on individual fully corrected images in the energy bands 0.2(0.8)–1.0 keV, 1.0–1.4 keV, and 1.4–4.0 keV. The hot gas emission appearing in green sticks out in this representation compared to the large number of point sources (mostly active galactic nuclei, AGN, in the background but also some foreground stars), which often appear redder or bluer. Furthermore, in the inset we show a zoom into the core region using all the useful XMM-Newton data available (1.6 Ms total flare-free exposure time of archival observations). The fully corrected and adaptively smoothed XMM-Newton RGB image is constructed in the energy bands: red: 0.3–0.7 keV, green: 0.7–1.5 keV, blue: 1.5–4.0 keV. The same features and sources are visible in both images with XMM-Newton showing more detail and sharpness in the innermost regions and eROSITA extending the field-of-view to beyond  $R_{500}$ .

To further enhance the visualization of the position of the large-scale sloshing cold front (“Edge”) we employ the Gaussian gradient magnitude (GGM) filtering technique (Sanders et al. 2016, as implemented in SciPy, Virtanen et al. 2020) to the eROSITA image and show the result in Fig. 6.

The real power of eROSITA compared to all other X-ray telescopes in existence comes in through its sensitivity to large-scale low surface brightness features. Already the bottom image in Fig. 2 revealed the vast extent of warm-hot gas emis-

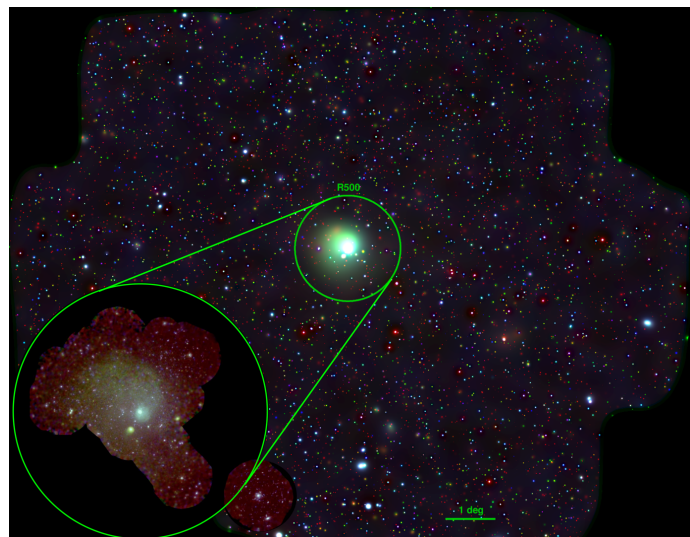


**Fig. 5.** Fully corrected, wavelet-filtered RGB images in the following energy bands: red: 0.2–1.0 keV, green: 1.0–1.4 keV, blue: 1.4–4.0 keV; linear scale. The lower left corner shows an XMM-Newton mosaic of the central region (see text for details).

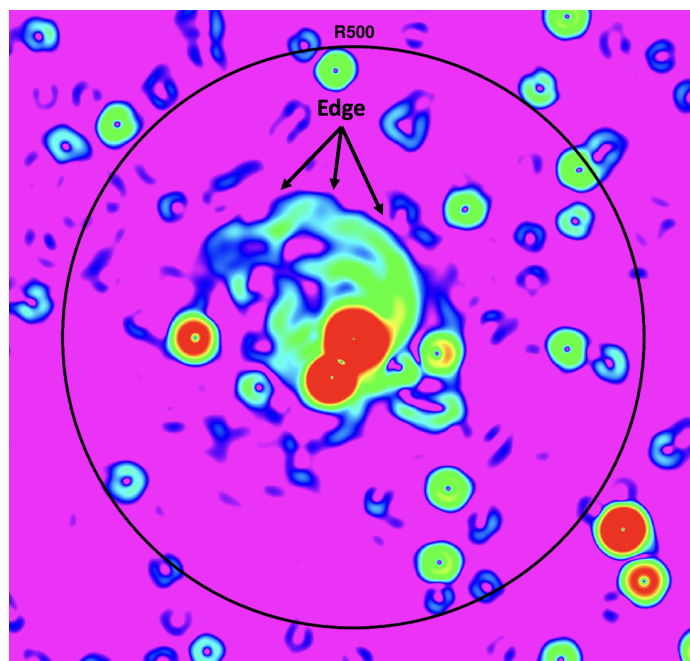


**Fig. 6.** GGM-filtered image in the energy band 0.2–2.3 keV; zoom into the central region; log scale. The large-scale edge spanning from the north-east to the north-west is prominent in this representation.

sion, dwarfing the emission visible in the huge XMM-Newton mosaic image shown in Fig. 5. Note that we do not expect the surface brightness fluctuations in the bottom image in Fig. 2 to be due to photon noise because of the wavelet-filtering process. Visual support for this expectation comes from comparing the eRASS:2 and eRASS3+eRASS4+eRASS5 images in Fig. A.1 in the appendix, which both show essentially the same features while coming from completely independent datasets. The quantitative analysis of the surface brightness profiles in different sectors follows below.

To make additional use of eROSITA’s energy resolution, we show in Fig. 7 an RGB image optimized to show low surface brightness fluctuations. Hot group and cluster gas emission is re-

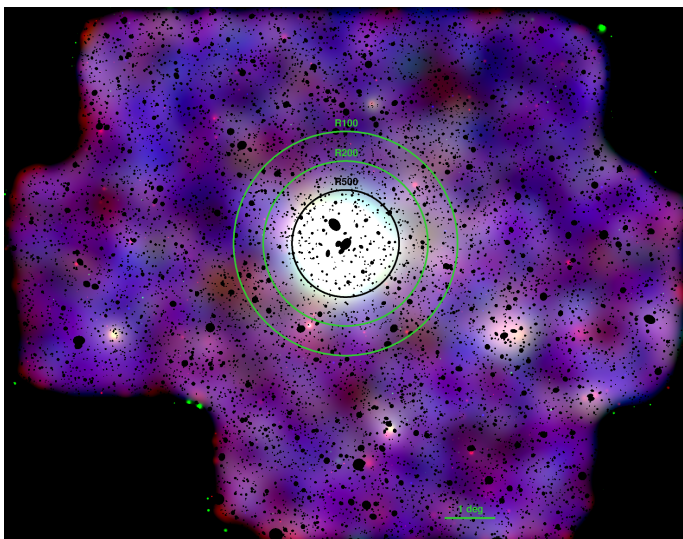


**Fig. 7.** As Fig. 5 but on log scale and sources of small extent excised; scale limits chosen to enhance low surface brightness fluctuations.

vealed in this image not only through its extent but additionally through its whitish color. Both images, Figs. 2 (bottom) and 7 demonstrate that the Fornax cluster emission extends not only beyond  $R_{500}$ , already unreachable by the XMM-Newton mosaic, but beyond  $R_{200}$  and actually beyond even the virial radius,  $R_{100}$ , in some directions. In these images, we discover finger-like emission extensions beyond  $R_{500}$  in particular towards the western and south-eastern directions (labeled “Finger 1, 2, and 3” in Fig. 2, bottom). These extensions appear to stretch out to well-beyond  $R_{100}$ , in particular “Excess 1 and 2.”

On the other hand, we do not see any obvious evidence in the X-ray surface brightness maps for the shock front predicted by Sheardown et al. (2018) south of NGC 1404. Below, we check quantitatively for features in the profiles in various sectors.

In principle, varying diffuse emission in our Milky Way or systematic uncertainties in the relative absorption correction can result in apparent surface brightness variations. Both effects would mostly be important at the softest energies  $<1$  keV. Therefore, we construct a hard band image (shown in Fig. B.1 in the appendix) and check if the emission features discussed above are robust. And, indeed, they are, lending confidence that they are not due to local effects.

The plots in Fig. 8 illustrate examples of surface brightness features discussed above. The uppermost plot simply shows how well eROSITA can recover already known features in the inner regions; i.e., a strong drop of emission just beyond  $R_{2500}$  – the “Edge” seen in Fig. 6. The next plot makes clear that “Excess 1 and 2” in the west-north-west beyond  $R_{100}$  discussed above have, indeed, a significantly higher surface brightness than the CXB level as there are many data points consistently above this level. Furthermore, it shows that our CXB level estimate is conservative because the surface brightness of the dark blue regions is even below our CXB level estimate. The next two plots show how the surface brightness drops abruptly and significantly at the edges of Finger 1 and 2; Finger 1 at  $R_{100}$  and Finger 2 between  $R_{200}$  and  $R_{100}$ .

We can now also search for the detached bow shock predicted by Sheardown et al. (2018) to lie 450–750 kpc south of NGC 1399; i.e., roughly in the range between  $R_{500}$  (393 kpc, 1.06 deg) and  $R_{100}$  (816 kpc, 2.22 deg). Since it is not clear where exactly such a shock would be located and given the complexity

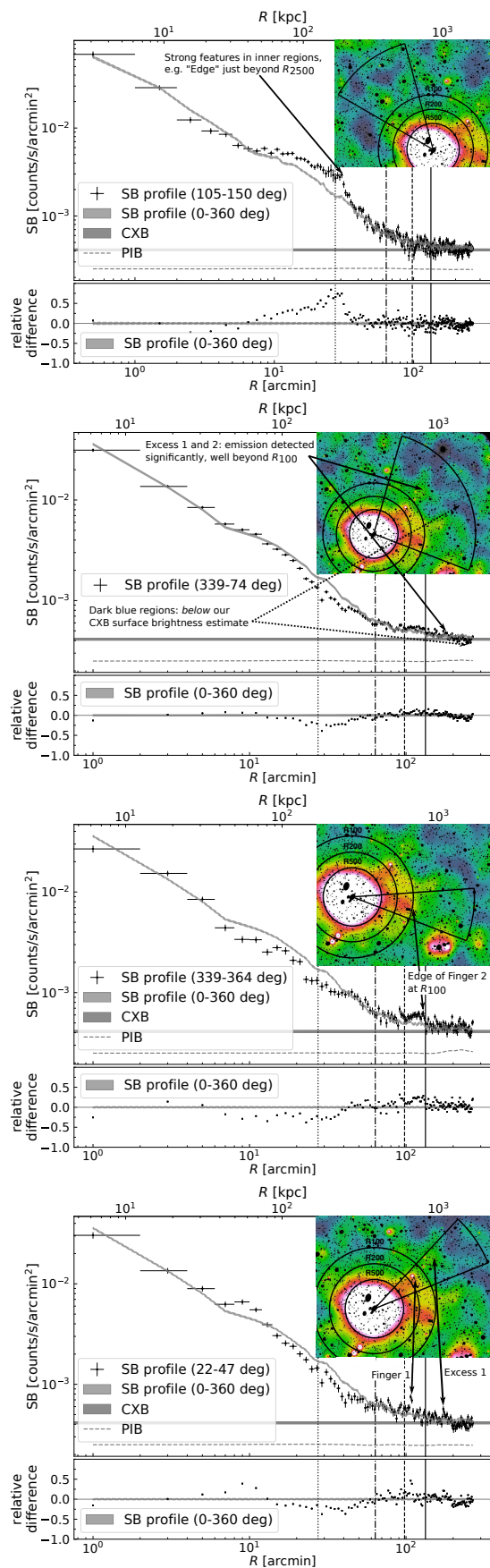


**Fig. 8.** Surface brightness profiles for different sectors with different features labeled.

of the two-dimensional emission in the outskirts, we start with a large sector and then look at smaller ones in different directions. Figure 3 (bottom) shows the southern 180 deg sector. No obvious surface brightness jumps that might be associated with a shock are obvious in the relevant radial range. Figures 9 and 10 show several more sectors. No obvious jump is present in the range 225–315 deg. In the 240–300 deg sector, there appear to be two peaks of emission surrounding  $R_{200}$ . However, consulting the surface brightness profiles of other sectors, in particular 225–270 deg and 240–270 deg, as well as the Finger 3 towards the south-east in Fig. 2, it becomes clear that these are two extended (note that each individual bin covers  $60''$ ; i.e., twice the eROSITA PSF) clumps of gas, not related to a shock front. On the other hand, the sector 180–270 deg does show a very weak indication of a surface brightness jump between  $R_{500}$  and  $R_{200}$ ; however, we consider it too weak, and the overall two-dimensional emission pattern too complex, to indicate a shock.

The sector 270–360 deg in Fig. 10 shows a bump starting around  $2R_{100}$ , likely related to the Fornax A group. In Fig. 11 we then show the surface brightness in a small sector towards and beyond the Fornax A group. It is clear that significant group emission spans at least 1 deg. Moreover, the indication for an apparent emission Bridge between the Fornax cluster and the Fornax A group is confirmed also in the surface brightness profile.

To get a better handle on the origin of these surface brightness extensions and excess regions, we compare to other tracers of the large-scale structure in and around the Fornax cluster in the next sections.

### 3.2. Distribution of cluster member galaxies

The most obvious additional tracer of structure is the distribution of galaxies in and around the Fornax cluster. As the Fornax cluster redshift is 0.005, we select all objects classified as galaxies from the NASA/IPAC Extragalactic Database (NED)<sup>4</sup> in the image area with a redshift less than 0.01. All of these are assumed to be member galaxies. With this selection we aim for high completeness of member galaxies. Since velocity dispersion measurements for the Fornax cluster reach  $\sigma_{\text{los}} \approx 400$  km/s and above (e.g., Drinkwater et al. 2001; Pota et al. 2018) we want to ensure to include all galaxies within at least  $3\sigma_{\text{los}} \approx 1200$  km/s, which corresponds to a  $z$  range of at least 0.001–0.009. Figure 12 shows the member galaxy distribution.

In the central region up to about  $R_{500}$ , the galaxy distribution exhibits an elongation in the east-west direction. On larger scales, well beyond  $R_{500}$ , one can notice a correlation of X-ray surface brightness excess regions and galaxy density. In particular, the Finger 1 and 2, and Excess 1, 2, and 3 seem to have their counterpart in the galaxy distribution. Moreover, also the X-ray emission Bridge towards the NGC 1316 group has an excess of galaxies; related to the lopsided distribution of Fornax A group dwarf galaxies towards the north-east discussed in Sect. 1 and (Su et al. 2021). The underlying reason for this offset between galaxy distribution and Fornax A intragroup gas might be related to the collisional gas lagging behind the collisionless galaxies in their common motion, e.g., due to ram pressure relative to the intracluster medium of the Fornax cluster outskirts; however, a more detailed investigation of this scenario is beyond the scope of this paper.

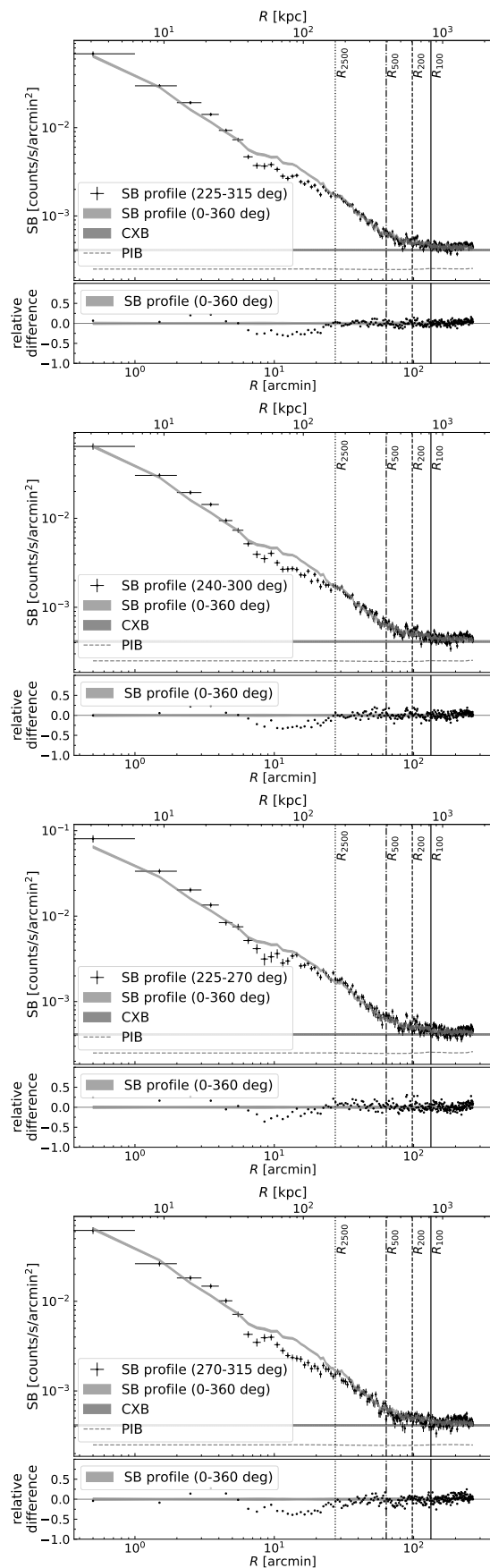


**Fig. 9.** Surface brightness profile sectors in the direction of the predicted bow shock.

<sup>4</sup> <https://ned.ipac.caltech.edu>

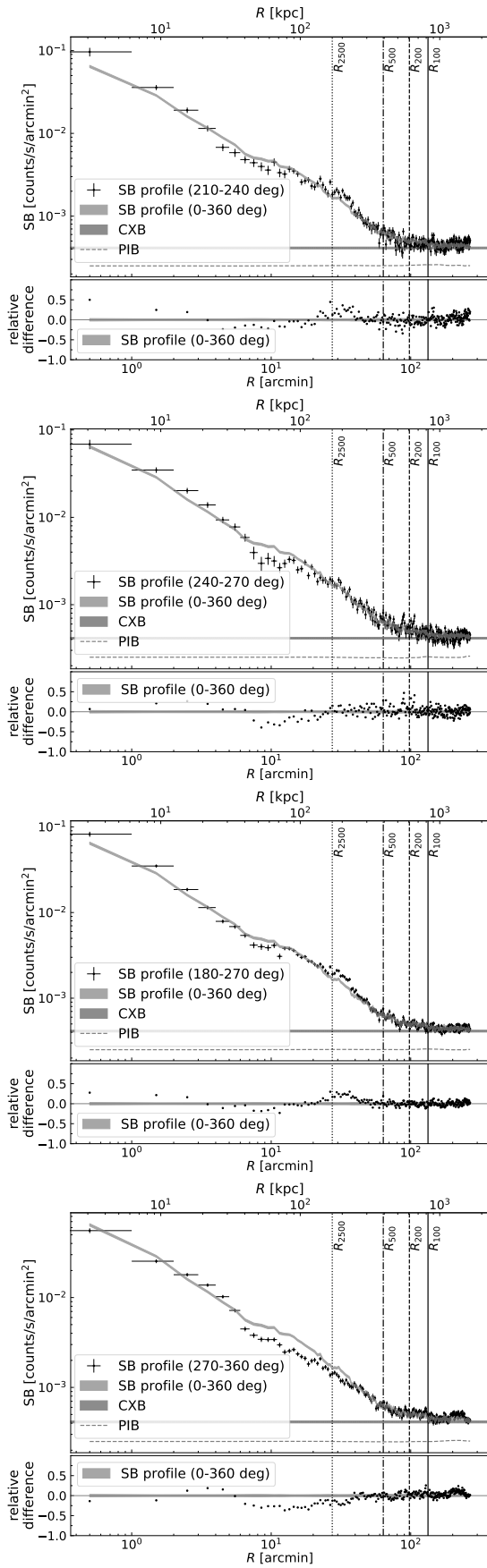


**Fig. 10.** Same as Fig. 9, showing several more sectors towards the predicted bow shock.

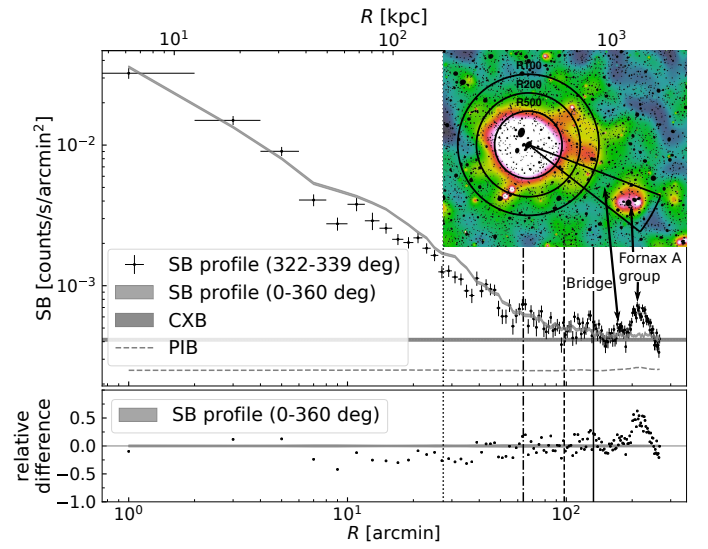


**Fig. 11.** Surface brightness profile in the direction of the Fornax A group.

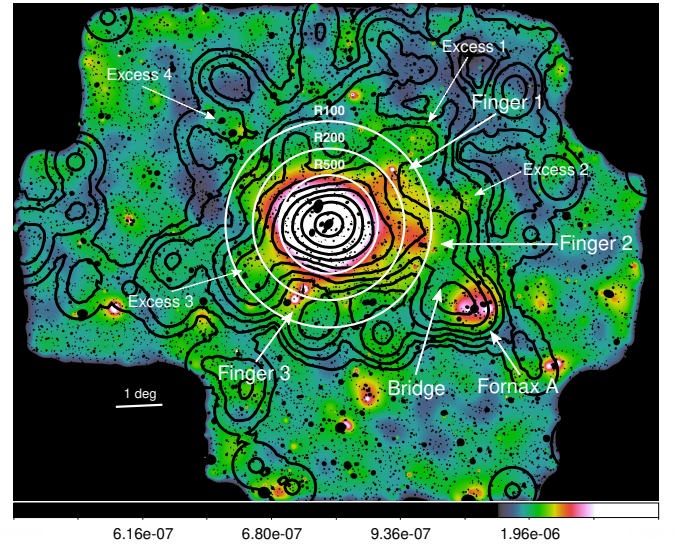


**Fig. 12.** Same as Fig. 2 but also showing density contours of galaxies at the Fornax cluster redshift from NED. Notice the overdensity of member galaxies at several of the regions of enhanced X-ray surface brightness in the outskirts, in particular to the west and south-east (marked as “Finger” and “Excess”) as well as the emission “Bridge” to the Fornax A galaxy group.

### 3.3. Distribution of intracluster ultra compact dwarf galaxies

As mentioned in Sect. 1, Drinkwater et al. (2001) argued based on their higher velocity dispersion that dwarf galaxies might be preferentially infalling. Tracers of disrupted dwarf galaxies are the so-called ultra compact dwarf galaxies (UCDs), the most massive of them being stripped nuclei of formerly nucleated dwarf ellipticals (Hilker et al. 1999; Drinkwater et al. 2003). In Fig. 13 we overlay the density of UCDs from Cantiello et al. (2020) onto the eROSITA image. Overall, we find a broad correlation between the UCD densities and the X-ray surface brightness. In particular, Finger 3 sticks out while the correspondence to the other features is weaker. The elongation in east-west direction in the central part also seems consistent with that observed in Fig. 12.

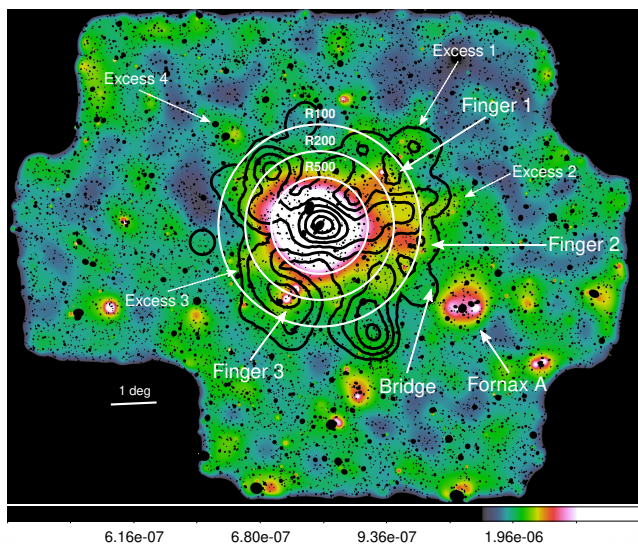


**Fig. 13.** Same as Fig. 12 but showing density contours of ultra compact dwarf (UCD) galaxies in the Fornax cluster from Cantiello et al. (2020). Notice the overdensity of UCD galaxies at regions of enhanced X-ray surface brightness in the outskirts, potentially marking preferred infall directions.

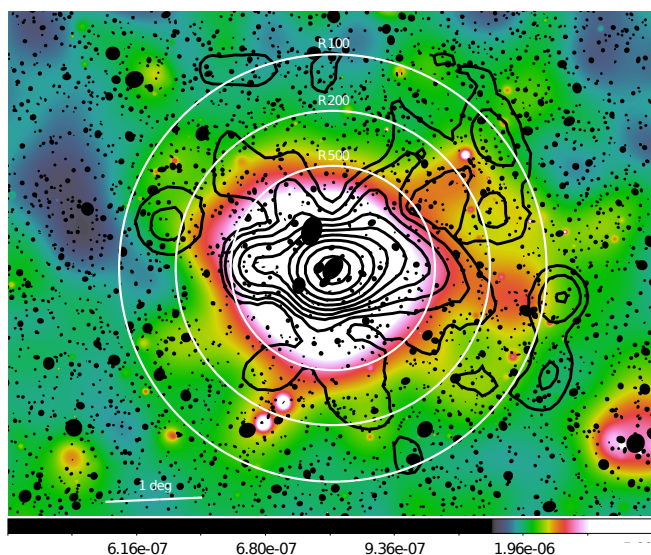


**Fig. 14.** Same as Fig. 12 but zoomed-in more and showing density contours of globular clusters in the Fornax cluster from Cantiello et al. (2020). The overdensities of globular clusters are in qualitative agreement with the potential infall directions marked by UCDs and shown in Fig. 13.

### 3.4. Distribution of intracluster globular clusters

Cantiello et al. (2020) also presented the spatial distribution of globular clusters in the Fornax cluster. The bright globular clusters in the inner region of  $\sim 1.5$  sq.deg around NGC 1399 have been confirmed spectroscopically as well (Chaturvedi et al. 2022). The globular cluster density is shown in Fig. 14 on top of the eROSITA image. Qualitatively, we find the same as for the UCD distribution – east-west elongation in the center and a correspondence with the X-ray surface brightness in the outer parts. Especially Finger 1 and 2 and Excess 1 and 2 and the Bridge seem to be traced approximately.

### 3.5. Distribution of background clusters and superclusters

eROSITA has discovered more than 12,000 galaxy clusters in more than 13,000 sq.deg across the western Galactic hemisphere (Bulbul et al. 2024; Kluge et al. 2024), including the region of the Fornax cluster. Therefore, we can expect about one background cluster per sq.deg, resulting in a large number to lie in the field under study here. As described in Sect. 2, we excised compact sources, which we expect to include background clusters as most of them will be at comparatively high redshift,  $z \gtrsim 0.1$  (the median redshift of the cluster catalog is 0.31), resulting in a small apparent size. Still, if there was an overdensity of clusters in a certain area, either just projected along the line of sight or forming a real supercluster, there might be significant summed emission present from their outskirts or from filaments connecting them. We want to test this in order to avoid incorrectly assigning excess emission to the outskirts of the Fornax cluster. To do so, we overlay in Fig. 15 the eRASS1 background clusters. Their redshifts are labeled and the circle sizes correspond to their  $R_{500}$  radii.

Several things can be noted in this Figure: (i) Our source detection indeed excises almost all of the background clusters, with a region size that is often comparable to  $R_{500}$ . While the source detection process here is very different, this is nonetheless not surprising given that we use data with five times the exposure time compared to eRASS1. It is also not surprising that there is a small fraction of clusters that we do not detect because (a) the purity of the eRASS1 catalog is estimated to be 86% (Bulbul et al. 2024) and (b) a few of them are very nearby ( $z \lesssim 0.05$ ) and, therefore, not compact. (ii) Some of the regions of enhanced surface brightness in the field indeed do correspond to overdensities of clusters, sometimes from a few at the same redshift, sometimes at different redshifts. While the clusters themselves are essentially all excised, there appears to be emission well beyond their  $R_{500}$  radii that, combined, is picked up by eROSITA. The cause of this apparent large-scale structure emission (e.g., WHIM surrounding clusters or an overdensity of undetected galaxies, AGN, or small groups of galaxies surrounding the clusters) will be studied in a future paper. (iii) Most of the main excess regions described in previous sections do *not* correspond to such cluster overdensities, making it unlikely they are due to projection of emission from the outskirts of background clusters. (iv) There are, however, a few X-ray excess regions that *do* show background cluster overdensities. Particularly interesting is that there are three clusters at the same redshift ( $\sim 0.31$ ) aligned almost perfectly with Finger 1 that points in the north-west direction (projected roughly at the Fornax  $R_{200}$ ). The projected extent is about 15 Mpc, in principle reasonable for a filament. Nonetheless, it seems unlikely that this emission finger is due to a background filament, especially because it would have to be a rather bright and thick ( $\sim 10$  Mpc) filament.

### 3.6. HI-tail galaxies

Cold gas stripping is widespread for galaxies falling into galaxy clusters (e.g., Cortese et al. 2021). Whether the same processes happen in lower mass galaxy groups is less clear. With a blind ATCA HI survey, Loni et al. (2021) did find evidence for neutral hydrogen removal within the virial region of the Fornax cluster. Using MeerKAT, Serra et al. (2023) recently increased the number of known HI-tail galaxies in Fornax from one to six, showing that ram pressure stripping can operate in this group, especially for galaxies that underwent interactions, thereby making their gas less bound. Four out of these six are located at projected



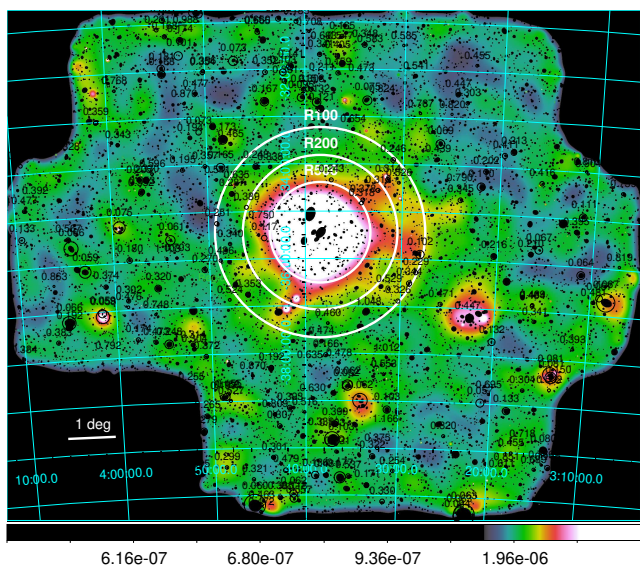


**Fig. 15.** Same as Fig. 2 but also showing the positions of background clusters from the eRASS1 catalog (Bulbul et al. 2024; Kluge et al. 2024). Redshifts are labeled and the circle radii correspond to  $R_{500}$ . See Figs. C.1 and C.2 in the appendix for zoomed-in versions.

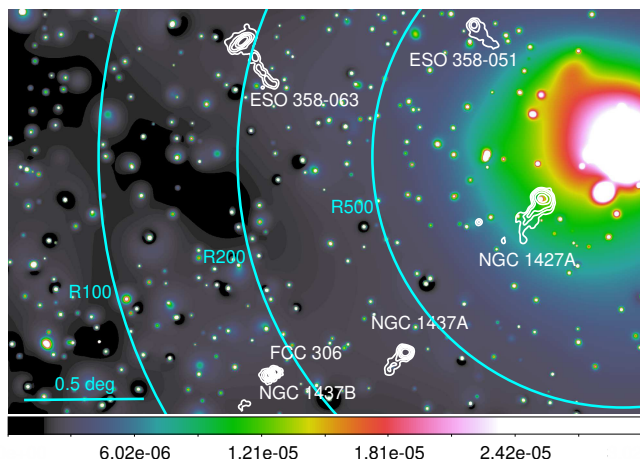


**Fig. 16.** Zoom into the eROSITA image shown in Fig. 2, top, plus atomic neutral hydrogen emission contours from MeerKAT from Serra et al. (2023), illustrating ram pressure stripping by the Fornax cluster ICM in action.

radii beyond  $R_{500}$ , thereby making their X-ray environment inaccessible to XMM-Newton or Chandra.

In Fig. 16, we show the HI contours from Serra et al. (2023) on top of the eROSITA image. None of the host galaxies themselves shows strong X-ray emission. All four galaxies are in a region where X-ray emission from the Fornax ICM is clearly detected by eROSITA, though. Intriguingly, the HI-tails for three of them (FCC 306, NGC 1437B, and NGC 1437A) are parallel to the south-eastern Finger 3 and coincident with an overdensity of possibly infalling UCDs (Fig. 13). The tail of NGC 1427A located inside  $R_{500}$  also points in the same direction. Furthermore, the tails of the two northern galaxies, ESO 359-063 and ESO 358-051 align with the direction towards Excess 4 and also seem coincident with a UCD overdensity.

In this context, it is interesting to note that Chaturvedi et al. (2024) have shown, by analyzing Fornax cluster-like halos in the Illustris TNG50 simulation, that stripped HI gas should exist

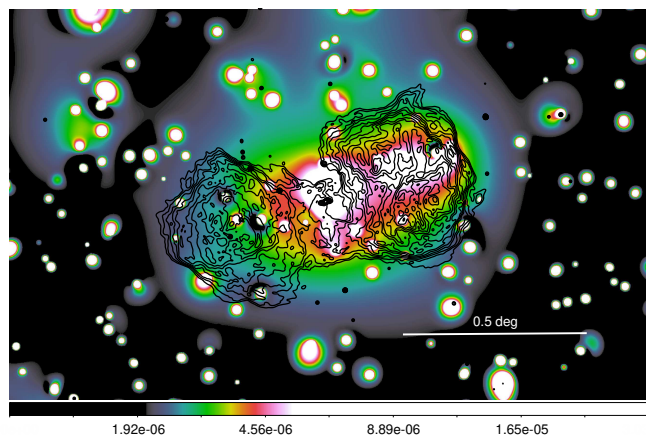


**Fig. 17.** Fully corrected, wavelet-filtered image in the energy band 0.2–2.3 keV zoomed in on the Fornax A radio galaxy (NGC 1316). Overlaid are MeerKAT 1.44 GHz contours from Maccagni et al. (2020). Note that the diffuse X-ray emission is aligned with the radio jet and lobe direction but extends further for a total linear size of at least 1 deg.

out to beyond the virial radius, with a non-negligible covering fraction.

### 3.7. NGC 1316

NGC 1316 is the central galaxy of a galaxy group that appears to be bound to the Fornax cluster and falling into it (Drinkwater et al. 2001). It also hosts Fornax A, a bright radio AGN exhibiting very extended lobes. In Fig. 17, we show the eROSITA X-ray surface brightness and overlaid on it the MeerKAT radio contours from Maccagni et al. (2020). One can notice that the elongation of the X-ray surface brightness aligns with that of the radio lobes. Furthermore, we see in this image that the X-ray emission extends much farther than the radio lobes. The total extent is clearly more than 1 deg. Actually, looking at Fig. 2, bottom, the total extent might well be 2 deg in this direction. This large extent, as well as the fact that the X-ray emission does not trace the radio lobes exactly, shows that the soft X-ray emission traced by eROSITA is dominated by thermal emission from the NGC 1316 intragroup gas instead of by inverse Compton scattering of the photon background on the relativistic electron population that gives rise to the synchrotron emission observed in the radio regime. This appears to be in contradiction to earlier studies that assume that at 1 keV all X-ray emission has a non-thermal origin (e.g., Persic & Rephaeli 2019). At higher energies  $\gtrsim 1.5$  keV, the non-thermal component has been shown by Suzaku spectral analysis to dominate instead (e.g., Tashiro et al. 2009).

Given the emission Bridge that connects NGC 1316 with the Fornax cluster that we have discovered (see Fig. 12), it actually becomes hard to determine at all where the NGC 1316 group emission ends and where the Fornax cluster emission begins.

### 3.8. SLOW comparison

The SLOW simulations (Sorice 2018; Dolag et al. 2023) aim to reproduce the local large-scale structure by convolving randomly generated initial conditions with observed large-scale structure data (Sorice et al. 2016). A direct consequence is a set of simulated counterparts for locally observed galaxy clusters (Hernández-Martínez et al. 2024) reproducing positions and

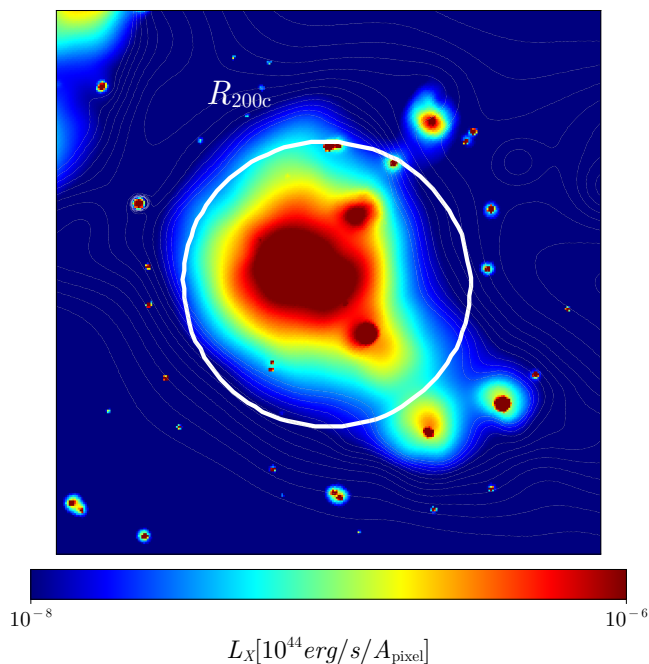


**Fig. 18.** The Fornax cluster and the Bridge to Fornax A as they appear in the X-ray band (0.1–2.4 keV) mock of the SLOW simulation of the local Universe (projection out to 350 Mpc). Also the “fingers” to the west seen in the eROSITA image are present (but see text). The grey contours indicate the gas density levels in the interval  $\rho = [0.8, 3.0] \times \rho(R_{200})$  in a 10 Mpc slice centered on the Fornax cluster. Based on Dolag et al. (2023); Hernández-Martínez et al. (2024).

general properties with good accuracy. Recent comparisons to observations (e.g., Dieltl et al. 2024) have shown especially the large-scale environment components of matched clusters such as massive neighbors and filaments to be matching well due to the reliable constraints on these scales. To test whether this holds for the relatively low-mass Fornax cluster we produce a mock observation of the simulated counterpart of the Fornax cluster in the SLOW simulation. We use the post-processing program SMAC (Dolag et al. 2005) to simulate X-ray emission in the 0.1–2.4 keV band. Additionally, we optimize the observer position for the mock observation so that Fornax is in exactly the correct sky position in order to eliminate projection uncertainties generated by the slight offsets from the true positions the simulation naturally generates.

In Fig. 18, we show the result of the SLOW simulation (Dolag et al. 2023; Hernández-Martínez et al. 2024) at the position of the Fornax cluster. Comparison to Fig. 2 shows, interestingly, that the Bridge towards Fornax A is also present. Furthermore, emission “fingers” to the west can be clearly seen in the image, which resemble those in the eROSITA image. Scrutinizing the simulation data, it turns out that, indeed, the finger to the south-west is co-located with the Fornax cluster. However, the emission in the image corresponding to the finger to the north-west is actually located 53 Mpc behind the Fornax cluster and is due to a projected galaxy group. When looking in detail at the grey gas density contours, though, a weak higher-density extension becomes obvious towards the north-west, right where the eROSITA image shows Excess 1.

## 4. Discussion and conclusions

With the new eROSITA observations, we have discovered X-ray emission from the Fornax cluster beyond  $R_{100}$  for the first time. The emission is not symmetric but instead shows preferred directions of higher X-ray surface brightness, as one might expect from gas infall along filaments. E.g., we find finger-like structures with sharp surface brightness drops around  $R_{100}$ , which then slowly fade out to much larger distances as regions of excess emission.

At different levels, the NED member galaxy, UCD galaxy, and globular cluster distributions are all correlated with the X-ray excess regions, and also the HI-tails of some member galaxies point in the same preferred directions. This offers the intriguing possibility that we are witnessing the ongoing growth of the Fornax cluster along preferred infall directions, consistently with the Fornax counterpart in the SLOW simulation. Alternatively, at least some of these features might be related to the ongoing minor merger with NGC 1404. However, we do not find obvious evidence for the shock front predicted by numerical simulations of this merger (Sheardown et al. 2018).

It is worth noting that no perfect agreement among the large-scale structure tracers may necessarily be expected. E.g., for the NED galaxy distribution no distinction is made here between newly infalling galaxies and galaxies that are already in full virial equilibrium with the gravitational potential. The UCD galaxy distribution, on the other hand, might be dominated by infalling galaxies. HI-tails clearly demonstrate infall and the projected direction is clear as well. Last but not least, for the X-ray surface brightness, all corrections have been performed. However, when comparing the surface brightness distribution with the distributions of the other tracers, one needs to be cautious because for none of the tracers based on individual objects (NED galaxies, UCDS, globular clusters, HI-tail galaxies) have any selection effects been taken into account. E.g., as the NED archive is not based on a complete catalog, no selection effect correction of galaxy density estimates can be performed. Therefore, there is uncertainty as different areas might have different sensitivities for the various tracers.

We have furthermore discovered a Bridge of X-ray emission towards NGC 1316, hosting Fornax A. This Bridge approximately coincides with a region of enhanced Faraday depth measured by Anderson et al. (2021), which itself also indicates the presence of a significant number of thermal electrons (and magnetic fields). The X-ray emission of the galaxy group around NGC 1316 itself extends well beyond 1 deg and is aligned with the radio lobes, indicating interaction between the relativistic and thermal electrons.

The detection of enhanced X-ray surface brightness in the outskirts of background clusters in overdense regions of the field implies that with eROSITA we start going beyond the detection of clusters as individual objects and instead see a Universe of continuous large-scale emission – as expected from cosmological simulations.

Based on the hard band (1.0–2.3 keV) image, we are confident that most of the X-ray features are not due to soft X-ray structure in our own Milky Way; still, it remains difficult to exclude with certainty that some of the X-ray excess regions may be due to foreground structure (see, e.g., the extreme cases of emission of the eROSITA Bubbles projected onto the outskirts of the Virgo and Centaurus clusters, McCall et al. 2024; Veronica et al. 2025). Correlations between X-ray excess regions and various other tracers of structure, like member galaxies and intra-cluster globular clusters, as employed here, do give confidence.

Final confirmation of the distance of individual excess regions may need to await high spectral resolution follow-up observations with *XRISM* (e.g., *XRISM Science Team* 2020), *HUBS* (e.g., Bregman et al. 2023), or even *NewAthena* (e.g., Nandra et al. 2013; Cruise et al. 2025) in order to pin down the redshifts of the excess regions from their X-ray emission lines.

*Acknowledgements.* TR and AV acknowledge support from the German Federal Ministry of Economics and Technology (BMWi) provided through the German Space Agency (DLR) under project 50 OR 2112. AV acknowledges funding by the Deutsche Forschungsgemeinschaft (DFG, German Research Foundation) – 450861021. We thank F. Maccagni and P. Serra for providing MeerKAT continuum contours of Fornax A and MeerKAT HI emission contours of ram pressure stripped galaxies. This work is based on data from eROSITA, the soft X-ray instrument aboard SRG, a joint Russian-German science mission supported by the Russian Space Agency (Roskosmos), in the interests of the Russian Academy of Sciences represented by its Space Research Institute (IKI), and the Deutsches Zentrum für Luft- und Raumfahrt (DLR). The SRG spacecraft was built by Lavochkin Association (NPOL) and its subcontractors, and is operated by NPOL with support from the Max Planck Institute for Extraterrestrial Physics (MPE). The development and construction of the eROSITA X-ray instrument was led by MPE, with contributions from the Dr. Karl Remeis Observatory Bamberg & ECAP (FAU Erlangen-Nuernberg), the University of Hamburg Observatory, the Leibniz Institute for Astrophysics Potsdam (AIP), and the Institute for Astronomy and Astrophysics of the University of Tübingen, with the support of DLR and the Max Planck Society. The Argelander Institute for Astronomy of the University of Bonn and the Ludwig Maximilians Universität Munich also participated in the science preparation for eROSITA. The eROSITA data shown here were processed using the eSASS software system developed by the German eROSITA consortium. This research has made use of the NASA/IPAC Extragalactic Database (NED) which is operated by the Jet Propulsion Laboratory, California Institute of Technology, under contract with the National Aeronautics and Space Administration. Partly based on observations obtained with XMM-Newton, an ESA science mission with instruments and contributions directly funded by ESA Member States and NASA. ChatGPT has been used to speed up writing some of the Python scripts, e.g., for plotting data. This work made use of astrometry.net.

## References

- Anderson, C. S., Heald, G. H., Eilek, J. A., et al. 2021, *PASA*, 38, e020
- Bertin, E. & Arnouts, S. 1996, *A&AS*, 117, 393
- Bregman, J., Cen, R., Chen, Y., et al. 2023, *Science China Physics, Mechanics, and Astronomy*, 66, 299513
- Brunner, H., Liu, T., Lamer, G., et al. 2022, *A&A*, 661, A1
- Bulbul, E., Liu, A., Kluge, M., et al. 2024, *A&A*, 685, A106
- Cantiello, M., Venhola, A., Grado, A., et al. 2020, *A&A*, 639, A136
- Chaturvedi, A., Hilker, M., Cantiello, M., et al. 2022, *A&A*, 657, A93
- Chaturvedi, A., Tonnesen, S., Bryan, G. L., et al. 2024, *ApJ*, 969, 28
- Cortese, L., Catinella, B., & Smith, R. 2021, *PASA*, 38, e035
- Cruise, M., Guainazzi, M., Aird, J., et al. 2025, *Nature Astronomy*, accepted, arXiv:2501.03100
- D’Abrusco, R., Cantiello, M., Paolillo, M., et al. 2016, *ApJ*, 819, L31
- Dietl, J., Pacaud, F., Reiprich, T. H., et al. 2024, *A&A*, 691, A286
- Dolag, K., Hansen, F. K., Roncarelli, M., & Moscardini, L. 2005, *MNRAS*, 363, 29
- Dolag, K., Sorce, J. G., Pilipenko, S., et al. 2023, *A&A*, 677, A169
- Drinkwater, M. J., Gregg, M. D., & Colless, M. 2001, *ApJ*, 548, L139
- Drinkwater, M. J., Gregg, M. D., Hilker, M., et al. 2003, *Nature*, 423, 519
- Ekers, R. D., Goss, W. M., Wellington, K. J., et al. 1983, *A&A*, 127, 361
- Freyberg, M., Perinati, E., Pacaud, F., et al. 2020, in *Society of Photo-Optical Instrumentation Engineers (SPIE) Conference Series*, Vol. 11444, *Space Telescopes and Instrumentation 2020: Ultraviolet to Gamma Ray*, ed. J.-W. A. den Herder, S. Nikzad, & K. Nakazawa, 114441O
- Hernández-Martínez, E., Dolag, K., Seidel, B., et al. 2024, *A&A*, 687, A253
- HI4PI Collaboration, Ben Bekhti, N., Flöer, L., et al. 2016, *A&A*, 594, A116
- Hilker, M., Infante, L., Vieira, G., Kissler-Patig, M., & Richtler, T. 1999, *A&AS*, 134, 75
- Iodice, E., Capaccioli, M., Grado, A., et al. 2016, *ApJ*, 820, 42
- Iodice, E., Spavone, M., Cantiello, M., et al. 2017, *ApJ*, 851, 75
- Jones, C., Stern, C., Forman, W., et al. 1997, *ApJ*, 482, 143
- Kluge, M., Comparat, J., Liu, A., et al. 2024, *A&A*, 688, A210
- Loi, F., Serra, P., Murgia, M., et al. 2025, *A&A*, 694, A125
- Loni, A., Serra, P., Kleiner, D., et al. 2021, *A&A*, 648, A31
- Maccagni, F. M., Murgia, M., Serra, P., et al. 2020, *A&A*, 634, A9
- Machacek, M., Dosaj, A., Forman, W., et al. 2005, *ApJ*, 621, 663
- Markevitch, M. & Vikhlinin, A. 2007, *Physics Reports*, 443, 1
- McCall, H., Reiprich, T. H., Veronica, A., et al. 2024, *A&A*, 689, A113
- Merloni, A., Lamer, G., Teng, L., et al. 2024, *A&A*, 682, A34
- Murakami, H., Komiyama, M., Matsushita, K., et al. 2011, *PASJ*, 63, S963
- Nandra, K., Barret, D., Barcons, X., et al. 2013, *Athena White Paper* [arXiv:1306.2307]
- Napolitano, N. R., Gatto, M., Spiniello, C., et al. 2022, *A&A*, 657, A94
- Ordenes-Briceño, Y., Eigenthaler, P., Taylor, M. A., et al. 2018, *ApJ*, 859, 52
- Persic, M. & Rephaeli, Y. 2019, *MNRAS*, 485, 2001
- Piffaretti, R., Arnaud, M., Pratt, G. W., Pointecouteau, E., & Melin, J.-B. 2011, *A&A*, 534, A109
- Pota, V., Napolitano, N. R., Hilker, M., et al. 2018, *MNRAS*, 481, 1744
- Predehl, P., Andritschke, R., Arefiev, V., et al. 2021, *A&A*, 647, A1
- Raj, M. A., Iodice, E., Napolitano, N. R., et al. 2020, *A&A*, 640, A137
- Reiprich, T. H. & Böhringer, H. 2002, *ApJ*, 567, 716
- Reiprich, T. H., Basu, K., Ettori, S., et al. 2013, *Space Sci. Rev.*, 177, 195
- Reiprich, T. H., Veronica, A., Pacaud, F., et al. 2021, *A&A*, 647, A2
- Sanders, J. S., Fabian, A. C., Russell, H. R., Walker, S. A., & Blundell, K. M. 2016, *MNRAS*, 460, 1898
- Schuberth, Y., Richtler, T., Bassino, L., & Hilker, M. 2008, *A&A*, 477, L9
- Serra, P., Maccagni, F. M., Kleiner, D., et al. 2023, *A&A*, 673, A146
- Sheardown, A., Roediger, E., Su, Y., et al. 2018, *ApJ*, 865, 118
- Smith Castellì, A. V., Cortesi, A., Haack, R. F., et al. 2024, *MNRAS*, 530, 3787
- Sorce, J. G. 2018, *MNRAS*, 478, 5199
- Sorce, J. G., Gottlöber, S., Yepes, G., et al. 2016, *MNRAS*, 455, 2078
- Starck, J. L. & Pierre, M. 1998, *A&AS*, 128, 397
- Su, A. H., Salo, H., Janz, J., et al. 2021, *A&A*, 647, A100
- Su, Y., Kraft, R. P., Roediger, E., et al. 2017a, *ApJ*, 834, 74
- Su, Y., Nulsen, P. E. J., Kraft, R. P., et al. 2017b, *ApJ*, 851, 69
- Sunyaev, R., Arefiev, V., Babyshkin, V., et al. 2021, *A&A*, 656, A132
- Tashiro, M. S., Isobe, N., Seta, H., Matsuta, K., & Yaji, Y. 2009, *PASJ*, 61, S327
- Veronica, A., Reiprich, T. H., Pacaud, F., et al. 2024, *A&A*, 681, A108
- Veronica, A., Reiprich, T. H., Pacaud, F., et al. 2025, *A&A*, 694, A168
- Virtanen, P., Gommers, R., Oliphant, T. E., et al. 2020, *Nature Methods*, 17, 261
- XRISM Science Team*. 2020, arXiv:2003.04962, arXiv:2003.04962
- Yeung, M. C. H., Freyberg, M. J., Ponti, G., et al. 2023, *A&A*, 676, A3
- Zheng, X., Ponti, G., Freyberg, M., et al. 2024, *A&A*, 681, A77

## Appendix A: Comparison of eRASS:2 and eRASS3+eRASS4+eRASS5 images

To check qualitatively if some of the features in the eROSITA images are caused by photon noise, we compare in Fig. A.1 two completely independent images. On the left hand side, we show the image using data from the first two eROSITA all-sky surveys (eRASS:2) and on the right hand side, the one created using data for the sum of the third, fourth, and fifth survey (eRASS3+eRASS4+eRASS5).

Essentially, the same features appear for both images here as those discussed in the main text for the full dataset (eRASS:5). In particular, Finger 1–3 and Excess 1–4 are present in both. This demonstrates visually that these surface brightness features are *not* caused by statistical fluctuations. This is expected given the noise-suppression properties of the wavelet-filtering process.

## Appendix B: Hard band eRASS:5 image

In Fig. 1 we showed that the Fornax cluster lies in a region with particularly stable background emission; background is low and does not show obvious strong variations. Still, given the scale of several degrees covered by the eROSITA image of the Fornax cluster, it is difficult to exclude emission variations in our Milky Way Galaxy as the underlying cause of the observed surface brightness fluctuations. Furthermore, varying absorption and uncertainties in our correction procedure may also induce apparent surface brightness variations. Both effects, emission from the low temperature plasma in our Galaxy and absorption by its neutral gas, are in practice only important well below a photon energy of 1 keV. Therefore, if one or both of these effects indeed gave rise to the features discussed in this paper, we would expect them to vanish in an image created using only photons with an energy of at least 1 keV. Therefore, we constructed a hard band image using the energy range 1.0–2.3 keV and show it in Fig. B.1.

Essentially, the same features appear in this image as in the broad band image. All Fingers and Excess regions are present. Also the Bridge to the Fornax A group becomes particularly clear in this energy band. This demonstrates that these surface brightness features are unlikely to be caused by varying emission or absorption effects in our Galaxy, as these are expected to be very weak above 1.0 keV.

## Appendix C: Close up views of background clusters

eROSITA can detect extended emission from hot gas not only nearby but out to redshifts even beyond one. In Fig. 15 we showed the distribution of background clusters on top of the eROSITA image of the Fornax cluster and the comparison was discussed in detail in Sect. 3.5. Here, we provide versions of the same image but zoomed into various areas to provide more detail.

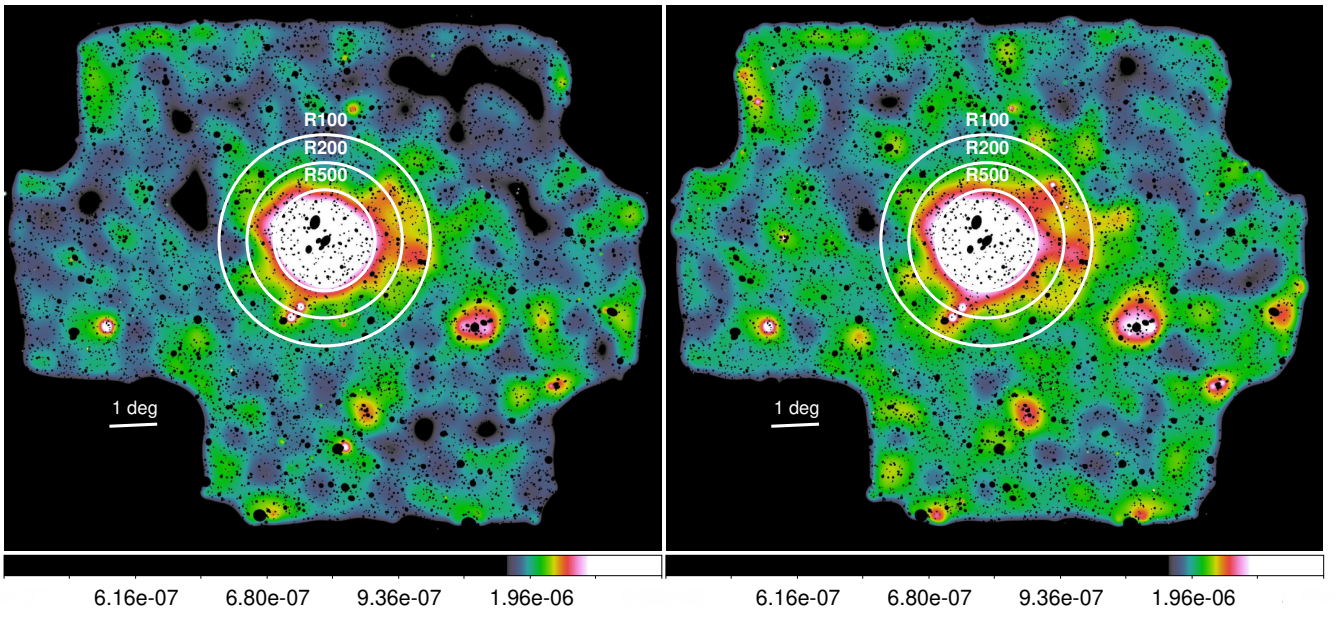


**Fig. A.1.** Same as Fig. 2 (bottom) but for eRASS:2 (left) and eRASS3+eRASS4+eRASS5 (right); i.e., two completely independent datasets.

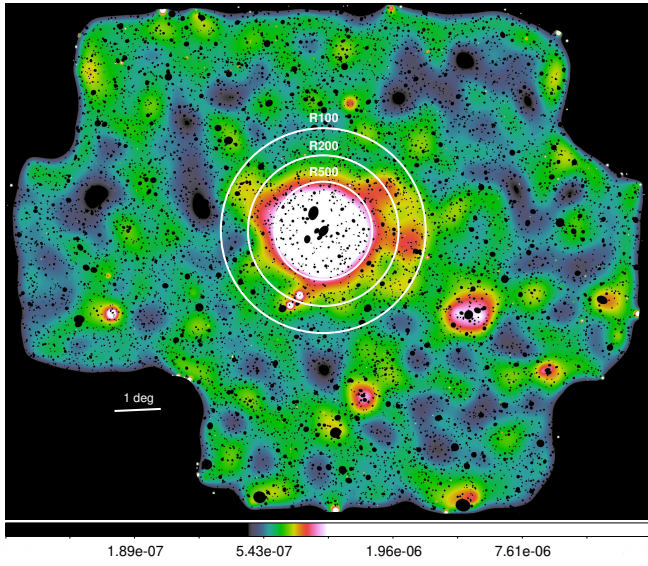


**Fig. B.1.** Same as Fig. 2 (bottom) but for the hard band, 1.0–2.3 keV.

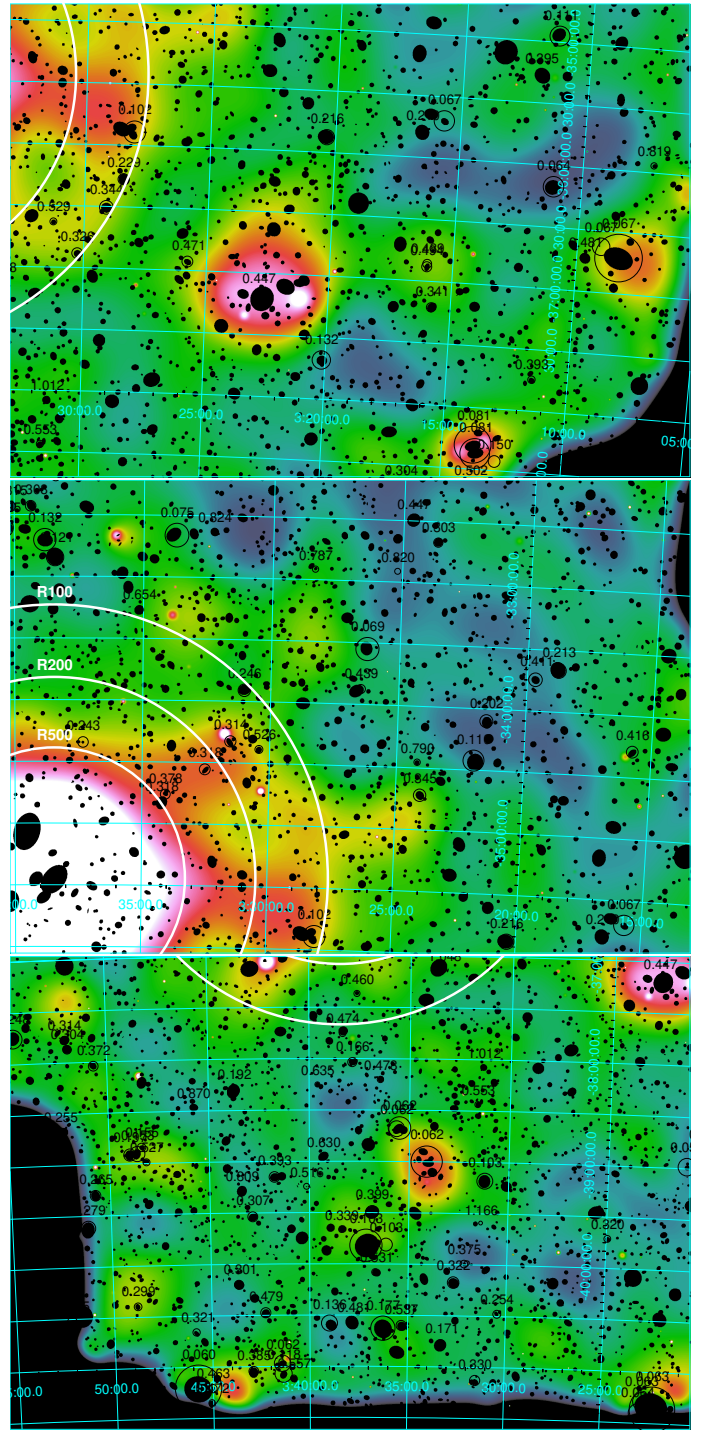
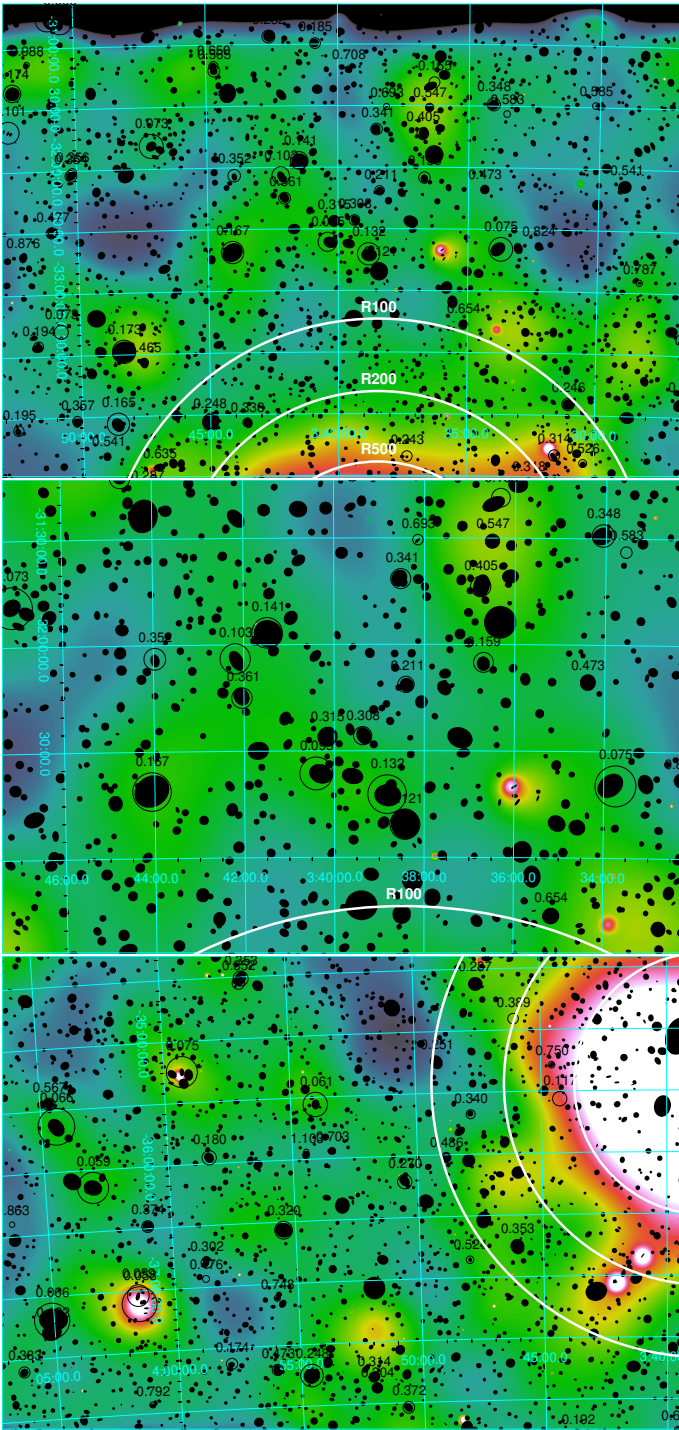


Fig. C.1. Same as Fig. 15 but zoomed into various areas.

Fig. C.2. Same as Fig. C.1 for a few more areas.